3-5-2012

Magnetohydrodynamic Flow of a Binary Electrolyte in a Concentric Annulus

M. Qin
University of Pennsylvania

Haim H. Bau
University of Pennsylvania, bau@seas.upenn.edu

Qin, M. and Bau, H. H. (2012). Magnetohydrodynamic flow of a binary electrolyte in a concentric annulus. *Physics of Fluids*, 24(3), 037101. doi: 10.1063/1.3689187

Magnetohydrodynamic Flow of a Binary Electrolyte in a Concentric Annulus

Abstract

We study theoretically magnetohydrodynamic (MHD) motion of a binary electrolyte in a concentric annulus subjected to a uniform, axial magnetic field. The annulus' cylindrical surfaces serve as electrodes. When a potential difference is imposed across the cylindrical electrodes, radial electric current flows in the solution and interacts with the axial magnetic field to induce a Lorentz body force that drives azimuthal fluid flow. When the annulus is infinitely long, a purely azimuthal flow (analogous to the classical Dean flow) is possible. We determine the velocity profile, ion concentration fields, and current density as functions of the electrodes' potential difference and study the linear stability of the azimuthal flow. Of particular interest is the effect of the ions' concentration fields on the centrifugal Dean instability. When the current is directed outwardly, electrochemical effects destabilize the flow, and the MHD flow loses stability at a Dean number much lower than its analogous, pressure driven flow. The supercritical flow consists of convective cells in the transverse plane. In contrast, when the current is directed inwardly, electrochemical effects stabilize the flow and the azimuthal flow is linearly stable for *all* Dean numbers. When the annulus is capped, purely azimuthal flow is no longer possible, and the flow in the annulus is always three-dimensional. In this case, the secondary flow is mostly driven by pressure gradients induced by the no-slip floor and ceiling. The intensity of the transverse convection depends then only weakly on the current's direction.

Disciplines

Fluid Dynamics | Physics

Comments

Qin, M. and Bau, H. H. (2012). Magnetohydrodynamic flow of a binary electrolyte in a concentric annulus. *Physics of Fluids*, 24(3), 037101. doi: 10.1063/1.3689187

Magnetohydrodynamic flow of a binary electrolyte in a concentric annulus

M. Qin and H. H. Bau[a)]
Department of Mechanical Engineering and Applied Mechanics, University of Pennsylvania, Philadelphia, Pennsylvania 19104-6315, USA

(Received 3 August 2011; accepted 2 February 2012; published online 5 March 2012)

We study theoretically magnetohydrodynamic (MHD) motion of a binary electrolyte in a concentric annulus subjected to a uniform, axial magnetic field. The annulus' cylindrical surfaces serve as electrodes. When a potential difference is imposed across the cylindrical electrodes, radial electric current flows in the solution and interacts with the axial magnetic field to induce a Lorentz body force that drives azimuthal fluid flow. When the annulus is infinitely long, a purely azimuthal flow (analogous to the classical Dean flow) is possible. We determine the velocity profile, ion concentration fields, and current density as functions of the electrodes' potential difference and study the linear stability of the azimuthal flow. Of particular interest is the effect of the ions' concentration fields on the centrifugal Dean instability. When the current is directed outwardly, electrochemical effects destabilize the flow, and the MHD flow loses stability at a Dean number much lower than its analogous, pressure driven flow. The supercritical flow consists of convective cells in the transverse plane. In contrast, when the current is directed inwardly, electrochemical effects stabilize the flow and the azimuthal flow is linearly stable for *all* Dean numbers. When the annulus is capped, purely azimuthal flow is no longer possible, and the flow in the annulus is always three-dimensional. In this case, the secondary flow is mostly driven by pressure gradients induced by the no-slip floor and ceiling. The intensity of the transverse convection depends then only weakly on the current's direction. © *2012 American Institute of Physics*. [http://dx.doi.org/10.1063/1.3689187]

I. INTRODUCTION

Magnetohydrodynamic (MHD) driven flow is of interest in many applications since one can induce fluid motion without a need for mechanical pumps and the flow velocity can be readily controlled by adjusting the current or the potential applied to electrodes.[1] Here, we consider MHD flow of a binary electrolyte confined in a conduit bent into a donut with an inner radius R_1 and an outer radius R_2. We use the cylindrical coordinate system (R, Θ, Z), where R, Θ, and Z are, respectively, the radial, azimuthal, and axial coordinates. The inner ($R = R_1$) and outer ($R = R_2$) surfaces of the annulus double-up as electrodes. The electrolyte is subjected to a uniform magnetic field directed parallel to the annulus' axis (Z). When a potential difference is applied across the electrodes, radial current flows in the solution. The current interacts with the axial magnetic field to produce an azimuthal, Lorentz body force, which, in turn, induces azimuthal flow.

When the cylindrical annulus is infinitely long (or when the annulus is finite and has slip floor and ceiling), purely azimuthal flow is possible.[2,3] The hydrodynamic stability of the analogous, pressure–driven flow in a concentric, infinitely long annulus was originally studied by Dean[2] and is referred to in the fluid mechanics literature [i.e., Ref. 3] and in this paper as the Dean problem. The flow stability can be characterized with the Dean number $\mathrm{Dn} = \mathrm{Re}(\mathrm{d}/\mathrm{R}_1)^{1/2}$. Here, $\mathrm{Re} = \left|\overline{V}\right| d \big/ \nu$ is the Reynolds number; $\overline{V}$ is the average azimuthal velocity; ν is the kinematic viscosity; and d

a)Electronic mail: bau@seas.upenn.edu.

$= R_2 - R_1$ is the width of the gap between the two cylinders. When the Dean number is smaller than a critical value, the azimuthal flow is stable. When the Dean number exceeds its critical value, the purely azimuthal flow loses stability and gives rise to convective rolls in the transverse $R - Z$ plane.[4,5] As the Dean number increases above a critical value so does the complexity of the flow.[6] When the height of the annulus is finite, purely azimuthal flows are not possible and transverse circulation exists for *all* Dean numbers.

Various researchers have studied pressure-driven flows in curved tubes with different cross sections such as circular,[7–13] elliptical,[14,15] square,[9,11,16] and rectangular.[15,17–19] Since the annular geometry has applications in heat exchangers, the associated convective heat transfer has also been studied.[20–23] Since pressure-driven flow in a perfectly closed loop cannot be generated in practice, by necessity, the closed loop approximates spiral geometry.[17]

In contrast, MHD flow provides a practical means of propelling fluids in a closed loop.[24,25] Various researchers[26–33] have studied the stability of annular MHD flow of liquid metals and have found that the magnetic field provides a stabilizing effect and suppresses the evolution of secondary flows.

Henceforth, the problem of MHD flow of electrolyte solutions in a concentric annulus and its stability has not been addressed. The case of electrolyte solutions is significantly different than that of liquid metals as the flow patterns affect the ion concentration fields, which, in turn, affect the local electric conductivity.[34] These types of problems are of interest among other things, in electroplating, where it is desirable to maintain unidirectional (azimuthal) flow to assure plating uniformity and avoid secondary flows that may cause non-uniform material deposition,[35] and in liquid gyroscopes for navigation systems.[36]

More generally, in recent years, there has been a growing interest in studying the interplay between hydrodynamic stability and electrochemistry. Volgin and Davydov[37] have reviewed the literature pertaining to the electrochemical Rayleigh-Benard problem. In this paper, we study for the first time the MHD motion of a binary electrolyte in an annulus and its stability characteristics. The paper is organized as follows. Section II introduces the mathematical model. Section III derives a closed-form solution for the current flux, concentration distributions, and velocity fields in an infinitely long annulus. Section IV examines the linear stability of the azimuthal flow derived in Sec. III and delineates why electrochemical effects destabilize the azimuthal flow when the current is directed outwardly and stabilize the azimuthal flow when the current is directed inwardly. Section V describes the MHD flow in a finite-height, annular conduit. Section VI concludes.

II. MATHEMATICAL MODEL

Consider a binary electrolyte $M_x^{z_1} A_y^{z_2}$ confined between two concentric cylinders of radii R_1 and R_2 ($R_2 > R_1$). M^{z_1} is the metal ion and A^{z_2} is the anion. $d = R_2 - R_1$ is the gap between the cylinders. We consider both the case when the annulus is infinitely long and when it has a finite length L. The cylinders' surfaces in contact with the liquid are coated with metal M (same material as the cations) and serve as electrodes. We use the cylindrical coordinate system (R, Θ, Z) with its origin at the cylinders' center. The symbols $\mathbf{e}_R$, $\mathbf{e}_\Theta$, and $\mathbf{e}_Z$ denote, respectively, unit vectors in the radial (R), azimuthal (Θ), and axial (Z) directions (Figure 1). The electrolyte is subjected to a uniform magnetic field $\mathbf{B} = -B\mathbf{e}_Z$. When a potential difference is imposed between the pair of electrodes, electric current flux $\mathbf{J}$ is transmitted in the solution. The electric current interacts with the magnetic field to produce a Lorentz body force, which, in turn, induces fluid motion. The electrolyte undergoes the backward reaction of $M^{z_1} + z_1 e^- \leftrightarrow M(s)$ at the anode and the forward reaction at the cathode. Due to Faradaic reactions at the electrodes' surfaces, the anode continuously dissolves and the cathode is electroplated. We consider sufficiently short times so that the geometry of the electrodes does not change appreciably during the process.

The ion concentrations satisfy the Nernst-Planck equation,[38]

$$\frac{\partial C_i}{\partial T^*} = -\nabla \cdot \mathbf{H}_i, (i = 1, 2), \tag{1}$$

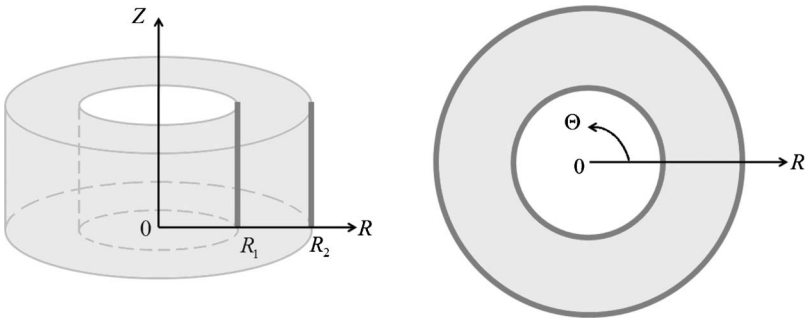

FIG. 1. A schematic depiction of the flow cell and the cylindrical coordinate system (R, Θ, Z). The electrolyte is confined in a concentric annulus with an inner radius R_1 and an outer radius R_2. The electrodes coincide with the cylindrical surfaces.

where C_1 and C_2 are, respectively, the concentrations of M^{z_1} and A^{z_2}; T^* is time;

$$\mathbf{H}_i = \mathbf{U}C_i - D_i^*\nabla C_i - z_i \upsilon_i F C_i \left(\nabla\Phi - \mathbf{U}\times\mathbf{B}\right) \tag{2}$$

is the ionic flux of species i; $\mathbf{U} = U\mathbf{e}_R + V\mathbf{e}_\Theta + W\mathbf{e}_Z$ is the velocity vector; D_i^*, z_i, and $\upsilon_i = D_i^*/(R_u T)$ are, respectively, the diffusion coefficient, valence, and mobility of species i; F is the Faraday constant; T is the absolute temperature; R_u is the ideal gas constant; and Φ is the electric potential. We adopt here the convention that regular fonts denote scalar quantities while bold letters represent vectors.

With the exception of very thin electric double layers next to the electrodes and other solid surfaces, the electro-neutrality condition requires that

$$\sum_{i=1}^{2} z_i C_i = 0. \tag{3}$$

The fluid motion satisfies the Navier-Stokes equation

$$\rho\left(\frac{\partial\mathbf{U}}{\partial T^*} + \mathbf{U}\cdot\nabla\mathbf{U}\right) = -\nabla P + \mu\nabla^2\mathbf{U} + \mathbf{J}\times\mathbf{B} - \tilde{\rho}g\hat{\mathbf{e}}_g. \tag{4}$$

The fluid is incompressible:

$$\nabla\cdot\mathbf{U} = 0. \tag{5}$$

In the Navier-Stokes equation, ρ is the uniform density in the absence of current. $\tilde{\rho} = \beta_1\left(C_1 - \bar{C}_1\right) + \beta_2\left(C_2 - \bar{C}_2\right)$ is the electrolyte's density deviation from ρ due to concentration variations. $\bar{C}_1$ and $\bar{C}_2$ are the uniform concentrations of ion 1 and ion 2 prior to the application of current. These quantities also represent volume averages of C_1 and C_2. Taking advantage of electroneutrality, (3) we can rewrite the density deviation as $\tilde{\rho} = \beta\left(C_1 - \bar{C}_1\right)$, where $\beta = \beta_1 - \frac{z_1}{z_2}\beta_2$. P is the hydrodynamic pressure that includes the hydrostatic term. μ is the dynamic viscosity. The term $\mathbf{J}\times\mathbf{B}$ in Eq. (4) is the Lorentz body force. $-\hat{\mathbf{e}}_g$ is a unit vector parallel to the gravity vector. g is the gravitational acceleration. In Eqs. (4) and (5), we invoked the Boussinesq's approximation and assume that the solution is dilute and its properties (except for the density in the body force) are independent of the ion concentrations and are uniform throughout the solution.

The electron exchange reactions at the surface of the electrodes are described by the Butler-Volmer kinetics,[39]

$$\mathbf{n}\cdot\mathbf{H}_1|_{R=R_1,R_2} = \frac{J_e}{F}\left\{\frac{C_1}{\bar{C}_1}\exp\left[\frac{-\alpha z_1 F}{R_u T}\left(V_{ext}^* - \Phi\right)\right] - \exp\left[\frac{(1-\alpha)z_1 F}{R_u T}\left(V_{ext}^* - \Phi\right)\right]\right\}. \tag{6}$$

Additionally, when the annulus is of a finite length,

$$\mathbf{n}\cdot\mathbf{H}_1|_{Z=0,L} = 0. \tag{7}$$

In the above, V_{ext}^* is the external potential difference imposed across the electrodes, $\bar{C}_1$ is the uniform cation bulk concentration before the current was applied, J_e is the exchange current flux, α is the

transfer coefficient, **n** is an outward unit vector, and Φ is the potential in the solution next to the electrode.

Mass conservation requires that

$$\int_{R_1}^{R_2}\int_{0}^{L} C_1 R dR dZ = \bar{C}_1 \frac{\left(R_2^2 - R_1^2\right) L}{2}. \tag{8}$$

All solid surfaces are impermeable to the inert species A^{z_2}:

$$\mathbf{n} \cdot \mathbf{H}_2|_{R=R_1,R_2;Z=0,L} = 0. \tag{9}$$

The fluid velocity satisfies non-slip conditions at all solid surfaces,

$$\mathbf{U}|_{R=R_1,R_2;Z=0,L} = 0. \tag{10}$$

The electric current flux

$$\mathbf{J} = F\sum_{i=1}^{2} z_i \mathbf{H}_i. \tag{11}$$

Taking advantage of electro-neutrality, we eliminate the potential from Eq. (1) to obtain the advection-diffusion equation

$$\frac{\partial C_i}{\partial T^*} = D^* \nabla^2 C_i - \mathbf{U} \cdot \nabla C_i, \tag{12}$$

where $D^* = (z_1 - z_2)\, D_1^* D_2^* \big/ \left(z_1 D_1^* - z_2 D_2^*\right)$ and

$$\nabla \cdot (C_i \nabla \Phi) = -\frac{R_u T}{F} z^* \nabla^2 C_i, \tag{13}$$

where $z^* = \left(D_1^* - D_2^*\right) \big/ \left(z_1 D_1^* - z_2 D_2^*\right)$.

Next, we convert the equations to a dimensionless form. To this end, we use the distance between the electrodes $d = R_2 - R_1$ as the length scale; $U_0 = \mu \big/ \rho d$ as the velocity scale; the viscous shear $\mu U_0 \big/ d$ as the stress/pressure scale; $d \big/ U_0 = \rho d^2 \big/ \mu$ as the time scale; the diffusive flux $H_0 = \bar{C}_1 D_1^* \big/ d$ as the ion flux scale; $J_0 = F H_0$ as the electric current density scale; the thermal potential $R_u T \big/ F$ as the electric potential scale; and the average concentration $\bar{C}_1$ of the species M^{z_1} as the concentration scale. Furthermore, we define the mean radius $R_0 = (R_1 + R_2) \big/ 2$. Below, with the exceptions of V_{ext} and D_i we express the dimensionless variables with the lower case version of their dimensional, upper case counterparts. The dimensionless applied potential is denoted as $V_{ext} = V_{ext}^* F \big/ R_u T$ and the dimensionless diffusion coefficient $D_i = D_i^* \big/ D_1^*$. The dimensionless time is denoted by t.

The dimensionless equations are

$$\frac{\partial c_i}{\partial t} = -\frac{1}{\mathrm{Sc}} \nabla \cdot \mathbf{h}_i, \tag{14}$$

$$\mathbf{h}_i = \mathrm{Sc} \cdot \mathbf{u} c_i - D_i \left[\nabla c_i + z_i c_i \left(\nabla \phi - \chi \mathbf{u} \times \mathbf{e}_z\right)\right], \tag{15}$$

and

$$\frac{\partial \mathbf{u}}{\partial t} + \mathbf{u} \cdot \nabla \mathbf{u} = -\nabla p + \nabla^2 \mathbf{u} + \kappa \left(j_r \mathbf{e}_\theta - j_\theta \mathbf{e}_r\right) - G_r \left(c_1 - 1\right) \hat{\mathbf{e}}_g. \tag{16}$$

In the above, $\mathrm{Sc} = \nu \big/ D_1^*$ is the Schmidt number and $\chi = \nu B F \big/ R_u T$ is the Lorentz number. $\kappa = J_0 B d^2 \big/ \mu U_0 = \rho F d^2 B \bar{C}_1 D_1^* \big/ \mu^2$ is the ratio of the Lorentz force and the viscous shear. Gr $= \frac{\rho g \beta \bar{C}_1 d^3}{\mu^2}$ is the Grashof number. We estimate the magnitudes of the various dimensionless numbers using a few typical values for solution properties. When $\rho = 10^3$ kg/m^3, $\beta = 0.1$ kg/m^3, $\bar{C}_1 = 10^4$ mol/m^3, $d = 10^{-3}$ m, $\mu = 10^{-3}$Pa $\cdot$ s, $B = 0.4$ T, and $D_1^* = 10^{-9}$ m^2/s, the Lorentz number $\chi \sim 10^{-4}$ and one can neglect the induced electromagnetic force in Eq. (15); $\kappa \sim 1000$; and the

Grashof number $\mathrm{Gr} \sim 10^4$. When $j_r \sim 0.1$ (i.e., Figs. 13(a) and 13(b)), the concentration deviation $c_1 - 1 \sim 0.01$ and the magnitudes of the buoyancy force and the Lorentz force are comparable. Thus, as in many other electrochemical processes,[37,40] buoyancy effects may be significant. We do not consider buoyancy effects in this paper because we wanted to focus on centrifugal instabilities and because the inclusion of buoyancy would have required us to treat separately different orientations of the annulus with respect to the direction of the gravity vector. Strictly speaking, our analysis is valid for low gravity conditions. We also focus on the axisymmetric problem ($\partial/\partial\theta = 0$) and $j_\theta = 0$.

The boundary conditions for the ion fluxes $\mathbf{h}_i$ are

$$\mathbf{n} \cdot \mathbf{h}_1|_{r=r_1,r_2} = j_e \left\{c_1 \exp\left[-\alpha z_1 \left(V_{ext} - \phi\right)\right] - \exp\left[\left(1-\alpha\right) z_1 \left(V_{ext} - \phi\right)\right]\right\} \tag{17}$$

and

$$\mathbf{n} \cdot \mathbf{h}_2|_{r=r_1,r_2} = 0. \tag{18}$$

The electro-neutrality condition requires that

$$\sum_{i=1}^{2} z_i c_i = 0. \tag{19}$$

The electric current density is

$$\mathbf{j} = F \sum_{i=1}^{2} z_i \mathbf{h}_i. \tag{20}$$

Mass conservation requires that

$$\int_{r_1}^{r_2} \int_{0}^{l} c_1 r dr dz = r_0 l. \tag{21}$$

The dimensionless form of Eqs. (12)–(13) becomes

$$\frac{\partial c_i}{\partial t} = -\frac{1}{\mathrm{Sc}} \nabla \cdot \left(\mathrm{Sc} \cdot \mathbf{u} c_i - D \nabla c_i\right), \tag{22}$$

where $D = D^*/D_1^*$ and

$$\nabla \cdot \left(c_i \nabla \phi\right) = -z^* \nabla^2 c_i. \tag{23}$$

III. STEADY FLOW OF BINARY ELECTROLYTE IN AN INFINITELY LONG ANNULUS ($l \to +\infty$)

The Dean problem of pressure-driven flow between two concentric cylinders has been studied extensively. Here, we consider the analogous MHD flow. While the Dean problem cannot be realized in a concentric annulus, the MHD flow can. When the flow is one-dimensional, the MHD flow is equivalent to pressure-driven flow[34] and we can adopt the classical solution for Dean flow.[41] We use the subscript "b" to denote the various dependent variables associated with the purely azimuthal flow.

Since the electric current is divergence-free, the electrical current flux

$$j_{r,b}\left(r\right) = \frac{j^* r_0}{r}. \tag{24}$$

In the above, $j^* = j_{r,b}(r_0)$ is the current flux at the mid-distance ($r_0 = r_1 + 1/2$) between the electrodes. The azimuthal velocity is

$$v_b\left(r\right) = \frac{\kappa j^* r_0}{2} r \left[\frac{1 - \left(r_2/r\right)^2}{1 - \left(r_2/r_1\right)^2} \ln\frac{r_2}{r_1} - \ln\frac{r_2}{r}\right]. \tag{25}$$

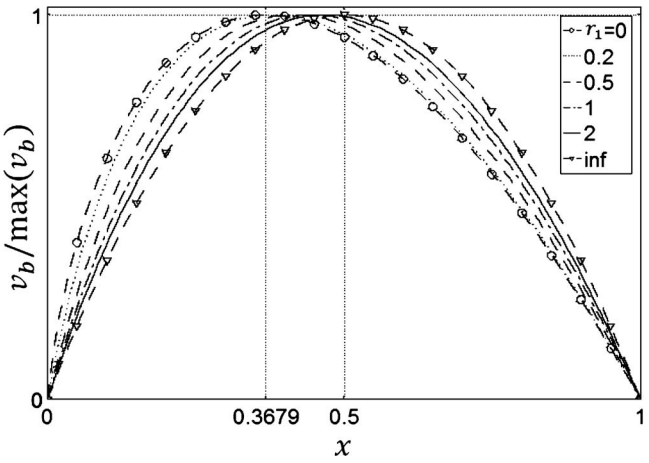

FIG. 2. The azimuthal velocity v_b (normalized with its maximum value) as a function of x when $r_1 = 0$, 0.2, 0.5, 1, 2, and ∞. The vertical lines at $x = 1/e$ and $x = 1/2$ correspond, respectively, to the positions of the velocity maximum when the curvature is large and small.

Figure 2 depicts v_b as a function of $x = r - r_1$ $(0 \le x \le 1)$ for various values of r_1. Digilov[42] derived Eq. (25) for MHD flow of liquid metals in the limit of a small Hartmann number. Since the magnitude of the current flux and thus the body force decreases as r increases, the velocity attains its maximum value in the interval $r_1 < r < r_0$ $(0 \le x \le 0.5)$. When $r_1 \ll 1$, the velocity maximum is attained at $x \to 1/e$, and Eq. (25) simplifies to

$$v_b(x) = \frac{\kappa j^*}{4} x \ln x. \tag{26}$$

As r_1 increases, the position of the velocity maximum shifts towards r_0 $(x = 0.5)$. When $r_1 \gg 1$ (small curvature), the velocity profile can be approximated as

$$v_b(x) = \frac{\kappa j^*}{2} x(1-x). \tag{27}$$

Expression (27) is identical to the velocity profile of pressure-driven (Poiseuille) flow between two long, parallel plates. The Reynolds number $\mathrm{Re} = |\bar{v}_b|$.

Next, we compute the concentration distribution. To this end, from Eqs. (14) and (15), we obtain

$$\frac{d}{dr}\begin{pmatrix} c_{1b} \\ c_{2b} \end{pmatrix} + \begin{pmatrix} z_1 c_{1b} \\ z_2 c_{2b} \end{pmatrix} \frac{d\phi_b}{dr} = \begin{pmatrix} -r_0 j^*/z_1 r \\ 0 \end{pmatrix}. \tag{28}$$

By introducing the scaled coordinate $\eta = \ln r$ $(\eta_1 = \ln r_1 < \eta < \ln r_2 = \eta_2)$, we convert Eq. (28) into a form similar to the one encountered in a planar geometry

$$\frac{d}{d\eta}\begin{pmatrix} c_{1b} \\ c_{2b} \end{pmatrix} + \begin{pmatrix} z_1 c_{1b} \\ z_2 c_{2b} \end{pmatrix} \frac{d\phi_b}{d\eta} = \begin{pmatrix} -r_0 j^*/z_1 \\ 0 \end{pmatrix} = \begin{pmatrix} A \\ 0 \end{pmatrix}. \tag{29}$$

In the above, the definition of the new variable A is apparent from the context. The solution of Eq. (29) together with the electroneutrality condition (19) and mass conservation (21) is

$$c_{1b} = 1 - \frac{A z_2}{(z_1 - z_2)}\left[\eta + \frac{1}{2} + \frac{r_1^2\eta_1 - r_2^2\eta_2}{2r_0}\right], \tag{30}$$

$$c_{2b} = -\frac{z_1}{z_2} c_{1b}, \tag{31}$$

and

$$\phi_b = G - \frac{1}{z_2}\ln\left[4r_0 z_1 (z_1 - z_2) c_{1b}\right]. \tag{32}$$

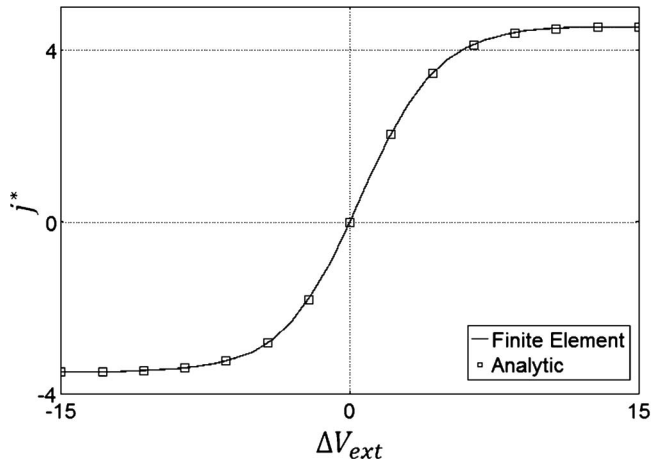

FIG. 3. The electric current flux as a function of the potential difference between the electrodes. The dimensionless inner radius $r_1 = 2$. The electrolyte is binary and symmetric, $z_1 = -z_2 = 1$. The dimensionless diffusion coefficients $D_1 = D_2 = 1$. Exchange current density $j_e = 10^3$. The symbols (squares) and the line correspond, respectively, to the analytical solution and the finite element simulation.

The constant G in Eq. (32) is determined by one of the electrodes' potentials.

When an electric potential difference is applied across the electrode pair, one needs to use the Butler-Volmer boundary conditions (17). Solving Eqs. (17) and (30)–(32) provide the current-voltage relation.

Figure 3 depicts the current flux as a function of the potential difference (ΔV_{ext}) across the electrode pair when $z_1 = -z_2 = 1$, $r_1/r_2 = 2/3$, $D_1 = D_2 = 1$, and the exchange current density $j_e = 10^3$. The symbols and the solid line correspond, respectively, to the analytical solution and the finite element solution of the Nernst-Planck equations. The excellent agreement between the numerical and analytical results partially verifies the numerical code that we will use later in the paper.

The positive (outward) $j_+^* = 4z_1(z_1 - z_2)(1-\delta)^2/z_2/(\delta^2 - 1 - 2\ln\delta)$ and the negative (inward) $j_-^* = 4z_1(z_1 - z_2)(1-\delta)^2/z_2/(\delta^2 - 1 - 2\delta^2\ln\delta)$ diffusion-limited electric current fluxes are, respectively, obtained by setting $c_{1b}(\eta = \eta_1) = 0$ and $c_{1b}(\eta = \eta_2) = 0$ in Eq. (30). In the above, $\delta = r_2/r_1 > 1$ is the radii ratio, $r_1 = 1/(\delta - 1)$, $r_2 = \delta/(\delta - 1)$, and $r_0 = (\delta + 1)/[2(\delta - 1)]$. The forward and backward limiting current fluxes differ in magnitude ($|j_+^*| > |j_-^*|$). For example, for the conditions of Figure 3, $-3.48 \le j^* \le 4.56$. Figure 4 depicts the ratio of the outward and inward limiting current fluxes $|j_+^*|/|j_-^*|$ as a function of the radii ratio δ. When $\delta \sim O(1)$, $|j_+^*|/|j_-^*| \sim (2\delta + 1)/3$ (dotted line in Figure 4). When $\delta \gg 1$, $|j_+^*|/|j_-^*| \sim (2\ln\delta - 1)$ (dashed line in Figure 4).

Figure 5 depicts the concentration c_{1b} as a function of the radial coordinate r under conditions of outward (dashed line) and inward (solid line) limiting current fluxes. In the inward current case, the concentration c_{1b} builds up next to the surface of the outer electrode and depletes next to the surface of the inner electrode. In the outward current case, the opposite is true. Since the surface area of the outer electrode is δ times larger than that of the inner electrode, the maximum concentration in the case of the outer directed current is larger than that in the case of the inward directed current. Accordingly, the concentration gradient in the inward current case is smaller than in the outward current case, providing less diffusive flux, and thus less net current flux.

Next, we consider the case of a small gap size ($r_1 \gg 1$), i.e., small curvature and nearly planar geometry. In this case, the electric current flux $j_{r,b} \sim j^*$ is independent of radial position. Equations (30)–(32) reduce, respectively, to

$$c_{1b} = 1 - \frac{j^*}{j_1}(2x - 1), \tag{33}$$

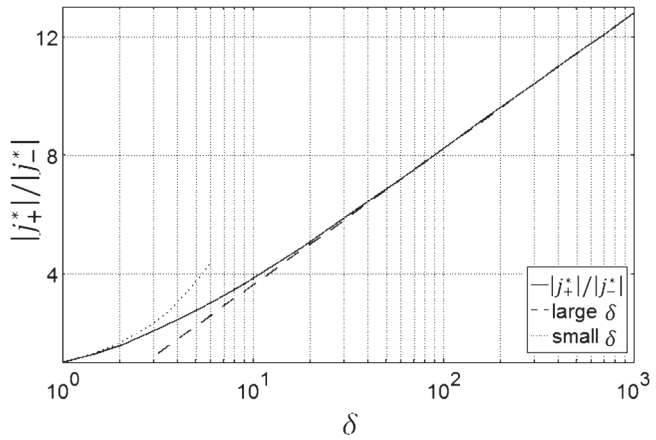

FIG. 4. The ratio between the outward and the inward limiting current fluxes ($|j_+^*|/|j_-^*|$) as a function of the radii ratio δ. $D_1 = D_2 = 1$, $z_1 = -z_2 = 1$, and $j_e = 10^3$. The dashed line ($2\ln\delta - 1$) corresponds to the large δ asymptote. The dotted line is the small δ asymptote $(2\delta + 1)/3$.

$$c_{2b} = -\frac{z_1}{z_2} c_{1b}, \tag{34}$$

and

$$\phi_b = G - \frac{1}{z_2} \ln (j_1 c_{1b}). \tag{35}$$

The potential difference across the gap

$$\Delta\phi = \phi_b (x = 0) - \phi_b (x = 1) = -\frac{1}{z_2} \ln \frac{j_1 + j^*}{j_1 - j^*}, \tag{36}$$

where $j_1 = 2z_1 (z_2 - z_1)/z_2$ is the dimensionless limiting diffusion-migration current.

With the aid of the Butler-Volmer boundary condition, we obtain the current-voltage relation. Figure 6 depicts the electric current flux as a function of the potential difference $\Delta V_{ext} = V_{ext}(x = 0) - V_{ext}(x = 1)$ when the exchange current density $j_e = 10^{-3}$, 10^{-2}, 10^{-1}, 1, 10, 10^2, and 10^3. $z_1 = -z_2 = 1$, $D_1 = D_2 = 1$, and $\alpha = 0.5$.

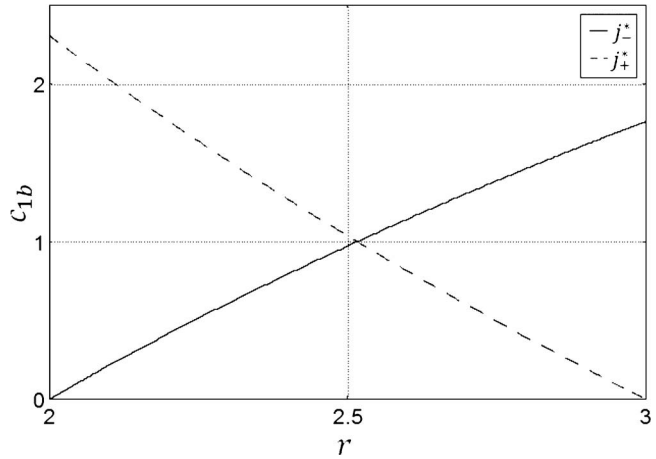

FIG. 5. The concentrations c_{1b} as functions of the radius r under limiting current conditions when the current is directed outwardly (dashed line) and inwardly (solid line). All other conditions are the same as in Figure 3.

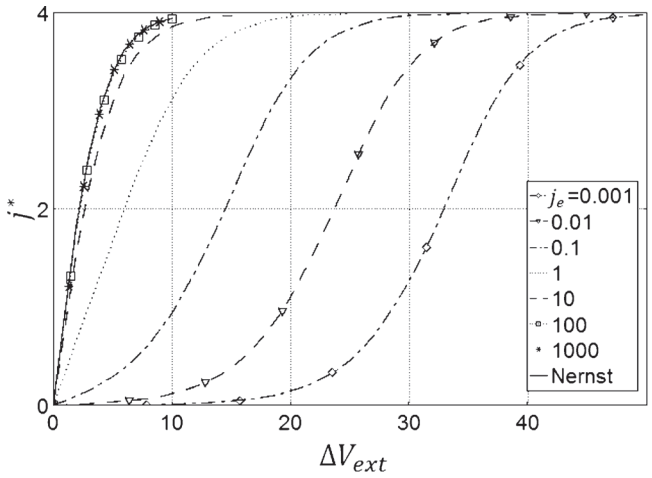

FIG. 6. The current flux as a function of the potential difference between the electrodes when the exchange current density $j_e = 10^{-3}$, 10^{-2}, 10^{-1}, 1, 10, 10^2, and 10^3. The curvature is neglected. Binary, symmetric electrolyte, $z_1 = -z_2 = 1$, and $D_1 = D_2 = 1$. Butler-Volmer electrode kinetics are used with $\alpha = 0.5$. The solid line corresponds to predictions obtained with the Nernst equation.

At large values of the exchange current density j_e, the Butler-Volmer relation (17) reduces to the Nernst equation. Then, we have at both boundaries ($x = 0$ and $x = 1$):

$$\phi_b = V_{ext} - \frac{1}{z_1} \ln c_{1b}. \tag{37}$$

With the aid of Eq. (36), the current-potential relation can be expressed as

$$j^* = j_1 \tanh \frac{z_2 \Delta V_{ext}}{2(z_2 - 1)}. \tag{38}$$

Figure 6 compares the predictions of the Nernst model (solid line) with the Butler-Volmer model when $j_e = 10^3$ (stars). Witness that both models provide nearly identical results when the exchange current is large.

IV. THE STABILITY OF THE AZIMUTHAL FLOW

In this section, we study for the first time, the linear stability of the MHD azimuthal flow in an infinitely long annulus. In the classical Dean problem, at sufficiently high azimuthal velocities, centrifugal accelerations destabilize the purely azimuthal flow and give rise to convective rolls in the transverse $r - z$ plane. In the electrochemical problem, the secondary flows modify the concentration distribution and, thus, the current flux, which, in turn, affects the Lorentz body force. Hence, we expect the stability characteristics of the electrochemical problem to significantly differ from those of the classical, pressure-driven Dean problem.

We restrict our analysis to an annulus with small curvature (small gap approximation). Following Dean's[2] original treatment, we neglect the effect of centrifugal accelerations on the base flow. Centrifugal effects are, however, accounted for in the perturbation equations.

We perturb the base flow variables (Eqs. (14)–(16)) with small disturbances, which we denote with the superscript tilde. For example, the concentration field assumes the form $c_i = c_{ib} + \varepsilon \tilde{c}_i$, where $\varepsilon \ll 1$, c_{ib} is the base solution (obtained in Sec. III), and $\tilde{c}_i$ is the first order perturbation. All other dependent variables are similarly perturbed. The perturbed variables are introduced into the equations and only terms of $O(\varepsilon)$ are retained. Furthermore, we decompose the perturbations into the normal modes

$$\tilde{c}_i = \hat{c}_i(x) \exp(\sigma t + ikz), \tag{39}$$

where σ is the growth rate; k is the wave number, and $\hat{c}_i$ is a function of x only. In the above, we assume that two-dimensional disturbances are less stable than three-dimensional ones. This assumption is consistent with Squire's theorem.[5,27] Accordingly, we consider only two-dimensional disturbances, and all the perturbation variables are independent of θ (i.e., $\partial/\partial\theta = 0$).

Invoking the small curvature approximation, $\partial/\partial\theta = 0$, and omitting the superscript tilde (ˆ), we obtain the $O(\varepsilon)$ linearized momentum equations,

$$\left(\mathrm{E}^2 - k^2 - \sigma\right)\left(\mathrm{E}^2 - k^2\right) g = vx\,(1-x)\,, \tag{40}$$

$$\left(\mathrm{E}^2 - k^2 - \sigma\right) v + \kappa j_x = \Lambda k^2 g\,(1-2x)\,, \tag{41}$$

and the continuity equation

$$\mathrm{E}u + ikw = 0. \tag{42}$$

The impermeability and no-slip boundary conditions at $x = 0$ and $x = 1$ are

$$g = \mathrm{E}g = v = 0. \tag{43}$$

For convenience, we introduced in the above the rescaled, radial velocity $g = u \cdot r_1/(\kappa j^* k^2)$. The operator $\mathrm{E} = d/dx$. $\Lambda = 72\bar{v}_b^2/r_1 = 72\mathrm{Dn}^2$, where Dn is the Dean number $\mathrm{Dn} = |\bar{v}_b|\sqrt{1/r_1}$. Equations (40)–(43) with $\kappa = 0$ are identical to the ones associated with the classical Dean problem.[5] The term κj_x is due to the Lorentz body force. This term couples the hydrodynamic problem with the electrochemical problem.

From Eqs. (22) and (23), we obtain, respectively, the linearized mass conservation equations for species 1:

$$\mathrm{E}^2 c_1 = \left(\frac{\mathrm{Sc}}{D}\cdot\sigma + k^2\right) c_1 + \frac{\mathrm{Sc}}{D}\cdot u\mathrm{E}c_{1b}. \tag{44}$$

The equation for the potential ϕ is

$$c_{1b}\mathrm{E}^2\phi = -z^*\left(\mathrm{E}^2 - k^2\right) c_1 + k^2 c_{1b}\phi - c_1\mathrm{E}^2\phi_b - \mathrm{E}c_1\mathrm{E}\phi_b - \mathrm{E}c_{1b}\mathrm{E}\phi. \tag{45}$$

The linearized flux of species i is

$$h_{ix} = \mathrm{Sc}\cdot u c_{ib} - D_i\mathrm{E}c_i - z_i D_i\left(c_{ib}\mathrm{E}\phi + c_i\mathrm{E}\phi_b\right). \tag{46}$$

The perturbation in the electric flux is

$$\begin{aligned} j_x &= \sum_{i=1}^{2} z_i h_{ix} = -\sum_{i=1}^{2} z_i D_i\left[\mathrm{E}c_i + z_i\left(c_{ib}\mathrm{E}\phi + c_i\mathrm{E}\phi_b\right)\right] \\ &= \left(D_2 - 1\right) z_1 E c_1 + \left(z_2 D_2 - z_1\right)\left(z_1 c_{1b} E\phi + z_1 c_1 E\phi_b\right). \end{aligned} \tag{47}$$

The perturbed concentrations satisfy the electro-neutrality condition

$$\sum_{i=1}^{2} z_i c_i = 0. \tag{48}$$

Below, we consider two types of boundary conditions. In the first instance, we assume that the current flux is specified at the electrodes' surfaces. This problem is mostly of theoretical interest as, in practice, it is difficult to control the local current flux. In the second instance, we specify the electrodes' potentials.

In each case, we solve the eigenvalue problem (40)–(48) and the appropriate electrochemical boundary conditions (to be specified later) with finite elements. Briefly, we select a wave number k and either the base current j^* or the applied potential ΔV_{ext}. In the first instance, we specify the perturbed current to be zero at the electrodes. In the second instance, the perturbed potential is zero at the electrodes' surfaces. The growth rate $\sigma(\mathrm{Dn}, k)$ is then calculated as a function of the Dean number Dn and the wave number k. The Dean number at marginal stability $\mathrm{Dn}_0(k)$ nullifies the real part of the growth rate, i.e., real $(\sigma(\mathrm{Dn}_0, k)) = 0$. We seek the *most dangerous* wave number k_0 that

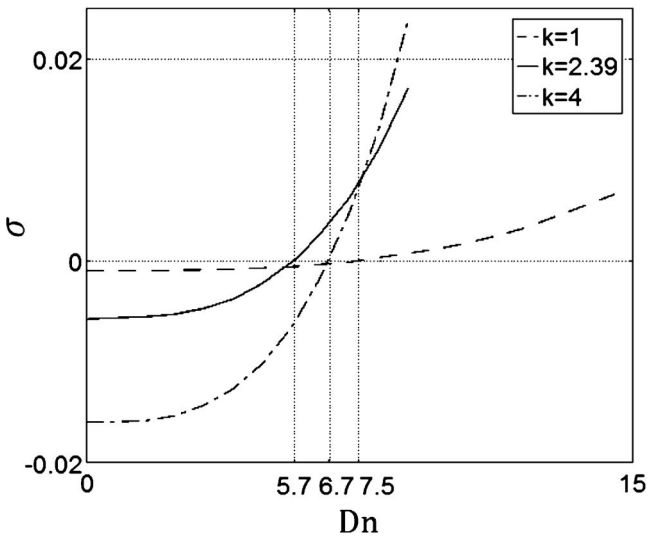

FIG. 7. The disturbance growth rate σ as a function of the Dean number when $k = 1$ (dashed line), 2.39 (solid line), and 4 (dashed-dotted line). Binary electrolyte, $z_1 = -z_2 = 1$, $D_1^* = D_2^* = 10^{-9}$ m^2/s, $\bar{C}_1 = 10^4$ mol/m^3, $R_1 = 0.5$ m, $R_2 = 0.505$ m, $B = 0.4$ T, $\rho = 10^3$ kg/m^3, and $\mu = 10^{-3}$ Pa $\cdot$ s.

minimizes $\mathrm{Dn}_0(k)$. In all our calculations, we find the growth rate σ to be real, i.e., the principle of exchange of stability holds.

To check our algorithm, we consider the hypothetical case of non-zero base velocity and $j_x = 0$. In this case, the κj_x term in Eq. (41) vanishes and the stability problem reduces to the classical Dean problem. Our finite element solution reproduces the well-known, classical results of $\mathrm{Dn}_0 = 35.92$ and $k_0 = 3.95$.[2,5] The bifurcating solution consists of convective rolls in the $r - z$ plane.

A. The case of controlled current

When the current flux is specified, the perturbation in the current is zero. The corresponding boundary conditions at $x = 0$, 1 are

$$\mathrm{E}c_1 = 0 \tag{49}$$

and

$$\mathrm{E}\phi = -\frac{c_1 \mathrm{E}\phi_\mathrm{b}}{c_{1b}}. \tag{50}$$

To determine the marginal stability curve, we calculate the growth rate σ as a function of the Dean number Dn for a given k. Figure 7 depicts σ as functions of Dn when $k = 1$ (dashed line), 2.39 (solid line), and 4 (dashed-dotted line). In all cases, σ is real. At criticality, $\sigma = 0$. This calculation was done for a binary and symmetric electrolyte, $z_1 = -z_2 = 1$, diffusion coefficients $D_1^* = D_2^* = 10^{-9}$m^2/s, $\bar{C}_1 = 10^4$ mol/m^3, $R_1 = 0.5$ m, $R_2 = 0.505$ m, $B = 0.4$ T, $\rho = 10^3$ kg/m^3, $\mu = 10^{-3}$ Pa $\cdot$ s, and $j^* > 0$.

Figure 8 depicts the Dean number at marginal stability (Dn_0) as a function of the wave number k for the same conditions as in Figure 7. The white and gray regions correspond, respectively, to stable ($\sigma < 0$) and unstable ($\sigma > 0$) states. Both the critical Dean number $\mathrm{Dn}_c = 5.7$ and the critical wave number $k_c = 2.39$ are smaller than their counterparts in the classical Dean problem. Interestingly, when $j^* < 0$, the base state is linearly stable for *all* values of the Dean number.

The linear stability results were compared with the results of numerical solutions of the full nonlinear equations. The computational domain consisted of a segment of the annulus with height of $0 < z < 2\pi/k$. Periodic boundary conditions are imposed in the $z-$ direction, i.e, all the dependent variables satisfy the condition: $a(x, z, t) = a(x, z + 2\pi/k, t)$. In the calculations, we used $k = 2.39$, 3.77, 5.05, and 7.12. When the calculations converged to the azimuthal base flow, the state was designated

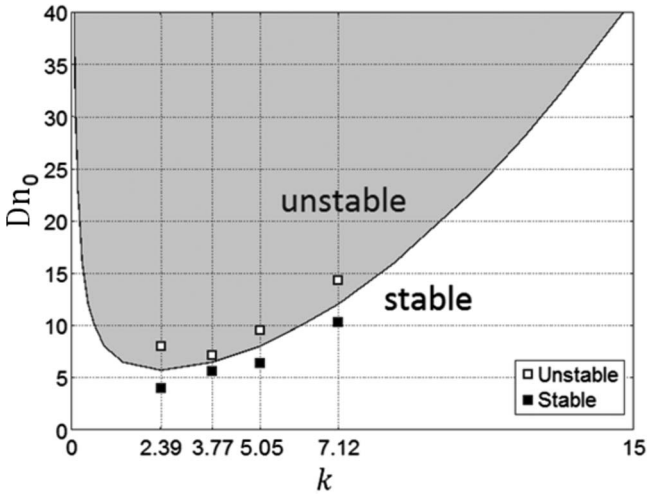

FIG. 8. The critical Dean number Dn_0 at the onset of instability, predicted by linear stability analysis, as a function of the wave number k. The electrodes' current is controlled. The white and gray regions correspond, respectively, to stable ($\sigma < 0$) and unstable ($\sigma > 0$) states. The symbols correspond to finite element solutions of the nonlinear equations. The solid and hollow symbols correspond, respectively, to subcritical (Dn^-) and supercritical (Dn^+) cases. The symbols are located at $\{k, Dn^-, Dn^+\} = \{2.39, 4.0, 8.0\}, \{3.77, 5.6, 7.2\}, \{5.05, 6.4, 9.7\}$, and $\{7.12, 10.5, 14.5\}$. The other conditions are the same as in Figure 7.

as stable. When the calculation converged to a state that consisted of convective cells in the $x - z$ plane, the state was designated as unstable. In all the cases considered here, the calculations eventually converged to a steady-state. The numerically identified stable and unstable states are denoted, respectively, with solid and hollow squares in Figure 8. The finite element solutions of the nonlinear equations are consistent with the predictions of the linear stability theory.

In all cases, consistent with the principle of exchange of stability, the transients were monotonic and no oscillations were observed. The finite element simulations suggest that the bifurcation from the azimuthal base flow to the three-dimensional flow is supercritical.

Figure 9 depicts a sample of the finite element solution of the nonlinear problem. The colors correspond to the concentration c_1. The lines are the streamlines of the secondary flow in the $r - z$

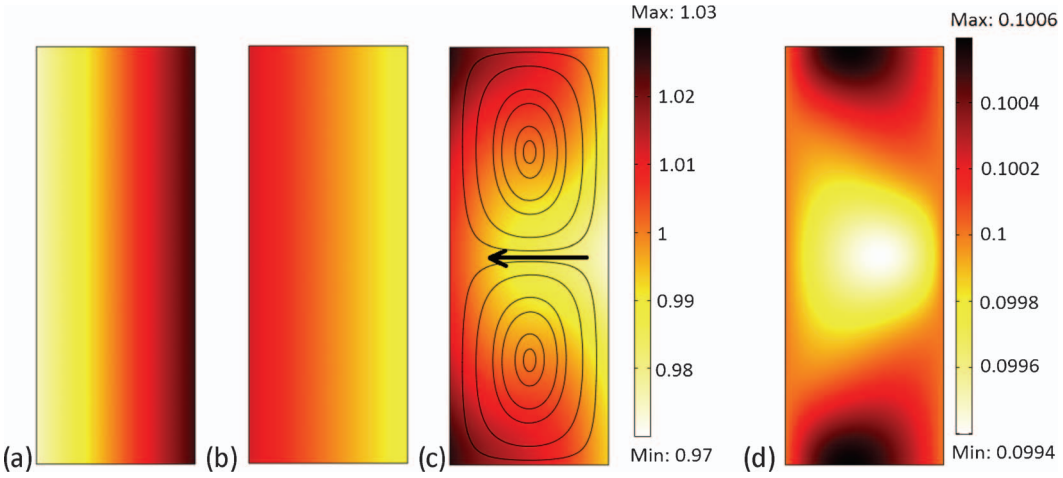

FIG. 9. (Color online) The concentration distribution of c_1 when (a) $j^* = -0.1$, $Dn = 8.04$; (b) $j^* = 0.05$, $Dn = 4.02$; and (c) $j^* = 0.1$, $Dn = 8.04$. The black solid lines in (c) are the streamlines associated with the secondary flow in the $r - z$ plane. The arrow shows the flow direction. (d) Electric current flux distribution for case (c). All the other parameters used are the same as in Figure 7.

plane. Figure 9(a) describes the case of inwardly directed current of magnitude $j^* = -0.1$ and Dn $\approx$ 8. Figure 9(b) depicts the case when the outward current $j^* = 0.05$ and Dn ≈ 4. This corresponds to a subcritical state (Dn $<$ Dn$_0$). Consistent with the predictions of the linear stability theory, there are no secondary flows in these cases, and the concentration distribution is uniform in the z direction. Figure 9(c) depicts the concentration and flow fields when the outward current $j^* = 0.1$ and Dn ≈ 8 are supercritical (Dn $>$ Dn$_0$). Consistent with the predictions of the linear stability analysis, convective rolls appear in the $r - z$ plane. The center of rotation is at $r \sim r_C$, where r_C is slightly larger than r_0. Figure 9(d) depicts the magnitude of the current flux under the same conditions as in Figure 9(c).

Figure 9(c) should be contrasted with Fig. 9(a). Although both cases correspond to the same Dean number, there are no secondary rolls present in the case of the inward current flow (a) while secondary flow is present in the case of the outward current flow (c). Consistent with the results of the linear stability theory, the nonlinear simulations predict an absence of secondary flows in the case of inward (negative) current.

In conclusion, when the base current is directed outwardly, the magnetohydrodynamic Dean problem is less stable than the pressure-driven one; but when the base current is directed outwardly, the opposite is true. So, what are the mechanisms that modify the stability characteristics of the classical Dean problem? To answer this question, we need to consider the ion concentration field in the annulus. When the current is directed outwardly, the ion concentration next to the inner surface (electrode) is larger than in the bulk of the solution. See Figs. 9(b) and 5. When due to the Dean (centrifugal) instability, fluid motion is induced away from the inner surface, the fluid advects ions into the bulk of the solution. This increases the local electric conductivity and the current flux. Witness the concentration "plumes" next to the bottom and top boundaries on the left-hand side of Figure 9(c). These plumes, in turn, enhance the Lorentz body force and increase the local azimuthal velocity and the resulting centrifugal acceleration, thereby enhancing the instability. For this reason, the magnetohydrodynamic Dean problem is less stable than the pressure-driven one.

When the base current is directed inwardly, the ion concentration next to the inner surface is smaller than in the bulk of the solution. See Figures 9(a) and 5. When centrifugal effects (Dean instability) cause a radial, outward convective disturbance, the advection reduces the local ion concentration and the corresponding electric conductivity away from the surface, which, in turn, causes a reduction in the Lorentz body force, the azimuthal velocity, and the centrifugal acceleration. Thus, the disturbance is suppressed. When the current is directed inwardly, electrochemical effects stabilize the azimuthal flow.

B. The case of controlled potential and Butler-Volmer boundary conditions

In this section, we consider the case when the potential difference between the electrodes is controlled. The injected current, as a function of the overpotential and the concentration, is given by the Butler-Volmer equation. The perturbed (linearized) Butler-Volmer boundary conditions at the electrodes' surfaces are

$$\mathbf{n}\cdot\mathbf{h}_{1x} = j_e\left\{\left(c_{1b}\alpha z_1\phi + c_1\right)\exp\left[-\alpha z_1\left(V_{ext} - \phi_b\right)\right] + \left(1-\alpha\right)z_1\phi\exp\left[\left(1-\alpha\right)z_1\left(V_{ext}-\phi_b\right)\right]\right\} \tag{51}$$

and

$$\mathbf{n}\cdot\mathbf{h}_{2x} = 0. \tag{52}$$

Together with Eq. (46), we obtain the boundary conditions

$$\mathrm{E}\phi = -\frac{h_{1x}}{\left(z_1 - z_2\right)c_{1b}} - \frac{c_1\mathrm{E}\phi_b}{c_{1b}} \tag{53}$$

and

$$\mathrm{E}c_1 = \frac{h_{1x}z_2}{z_1 - z_2}. \tag{54}$$

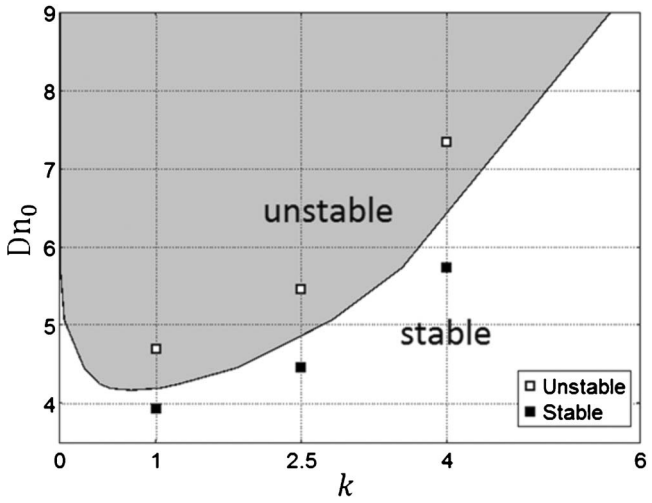

FIG. 10. The critical Dean number Dn_0 at the onset of instability as a function of the wave number. The annular conduit is infinitely long and electric potential is applied across the electrodes. The white and gray areas correspond, respectively, to stable ($\sigma < 0$) and unstable ($\sigma > 0$) cases. The hollow (Dn^+) and solid (Dn^-) symbols correspond, respectively to subcritical and supercritical cases. The symbols are located at $\{k, \mathrm{Dn}^-, \mathrm{Dn}^+\} = \{1, 3.93, 4.69\}$, $\{2.5, 4.46, 5.45\}$ and $\{4, 5.73, 7.34\}$. $j_e = 6 \times 10^{-3}$, $\alpha = 0.5$, $D_1^* = D_2^* = 10^{-9}$ m^2/s, $\bar{C}_1 = 10^4$ mol/m^3, $R_1 = 0.5$ m, $R_2 = 0.505$ m, $B = 0.4$ T, $\rho = 10^3$ kg/m^3, and $\mu = 10^{-3}$ Pa $\cdot$ s.

We solve the linear stability problem in a similar way to what we have done in Sec. IV A. Briefly, we specify the wave number and the Dean number and compute the eigenvalue $\sigma = \sigma(\mathrm{Dn}, k)$. As in the controlled current case, σ is always real and the principle of exchange of stability prevails. We then determine the value of $\mathrm{Dn}_0(k)$ that corresponds to $\sigma = 0$.

Figure 10 depicts the critical Dean number Dn_0 as a function of the wave number. The white and gray areas correspond to stable ($\sigma < 0$) and unstable ($\sigma > 0$) cases. When using the same electrolyte and conditions as specified in Figure 7 (outwardly directed base current), an exchange current density of $j_e = 6 \times 10^{-3}$ and $\alpha = 0.5$, we find that the critical Dean number $\mathrm{Dn}_0 = 4.17$ and the critical wave number $k_0 = 0.74$. As expected, since the potential boundary condition is less restrictive than the current flux condition (Sec. IV A), the critical Dean number in the potential-controlled case is smaller than in the current-controlled case. When the base current is directed inwardly, the azimuthal flow is stable for *all* Dean numbers.

The predictions of linear stability theory were compared with the results of the nonlinear, finite element simulations of Eqs. (14)–(16) with Butler-Volmer boundary conditions. The simulations were carried out for an annulus with height $l = 2\pi/k$, where $k = 1$, 2.5, and 4, and periodic boundary conditions at the top and bottom boundaries. The results of the numerical simulations are summarized with symbols in the stability diagram (Figure 10). The solid and hollow squares correspond, respectively, to subcritical ($\mathrm{Dn} = 3.93$, 4.46, and 5.73) and supercritical ($\mathrm{Dn} = 4.69$, 5.45, and 7.34) flows. The finite elements, nonlinear solutions are consistent with the predictions of the linear stability analysis.

C. The case of controlled potential with Nernst boundary conditions

When the electrode kinetics is rapid (large exchange current), the Butler-Volmer equations can be simplified to the Nernst boundary conditions (Eq. (37)). The perturbed boundary conditions are then

$$\phi = \frac{c_1}{z_1 c_{1b}} \tag{55}$$

and

$$\mathrm{E}c_1 = c_{1b}\mathrm{E}\phi + c_1\mathrm{E}\phi_b. \tag{56}$$

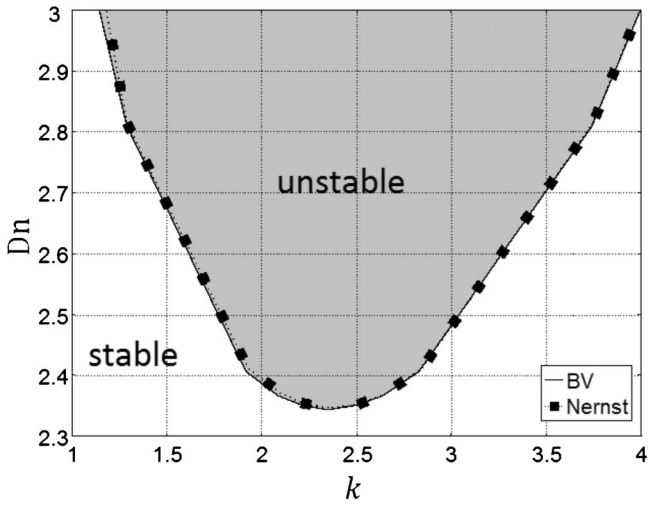

FIG. 11. The critical Dean number at the onset of instability as a function of the wave number. Controlled potential case. The white and gray areas correspond, respectively, to stable ($\sigma < 0$) and unstable ($\sigma > 0$) states. The dotted line with solid squares corresponds to the solution of the linear stability problem with Nernst boundary conditions. The solid line corresponds to the Butler-Volmer boundary conditions with $j_e = 10^3$ and $\alpha = 0.5$. All the electrolyte properties are the same as used for Figure 10.

To verify the linear stability analysis presented in Sec. IV B, we repeated the linear stability calculations using the simpler boundary conditions (55) and (56). All other parameters are the same as in Figure 10. Figure 11 depicts Dn_0 as a function of k as obtained using Butler-Volmer electrode kinetics when $j_e = 10^3$ (solid line) and the Nernst conditions (symbols). The agreement between calculations based on the Butler-Volmer kinetics and the Nernst kinetics is nearly perfect in the case of large exchange current density.

V. AN ANNULUS WITH A FINITE HEIGHT ($l < \infty$)

When the annulus has a finite height, purely azimuthal flow is not possible and secondary flows will always be present in the $r - z$ plane. We first examine the range of validity of the small gap approximation, which we have employed in Sec. IV. Then, we compare the intensity of the secondary flows between the cases of the outward and inward currents.

A. The range of validity of the small gap approximation

When the conduit's curvature is small, often the quasi-two-dimensional model (the Dean's approximation) is employed (Dean[2]) as we have done in Sec. IV. To assess the validity of the Dean approximation in our case, we compare the predictions of the two-dimensional model with the predictions of the axisymmetric model. The corresponding axisymmetric momentum equations are

$$u\frac{\partial u}{\partial r} + w\frac{\partial u}{\partial z} = -\frac{\partial p}{\partial r} + \frac{\partial^2 u}{\partial r^2} + \frac{\partial^2 u}{\partial z^2} + \frac{v^2}{r}, \tag{57}$$

$$u\frac{\partial v}{\partial r} + w\frac{\partial v}{\partial z} = \kappa j_r + \frac{\partial^2 v}{\partial r^2} + \frac{\partial^2 v}{\partial z^2}, \tag{58}$$

and

$$u\frac{\partial w}{\partial r} + w\frac{\partial w}{\partial z} = -\frac{\partial p}{\partial z} + \frac{\partial^2 w}{\partial r^2} + \frac{\partial^2 w}{\partial z^2}. \tag{59}$$

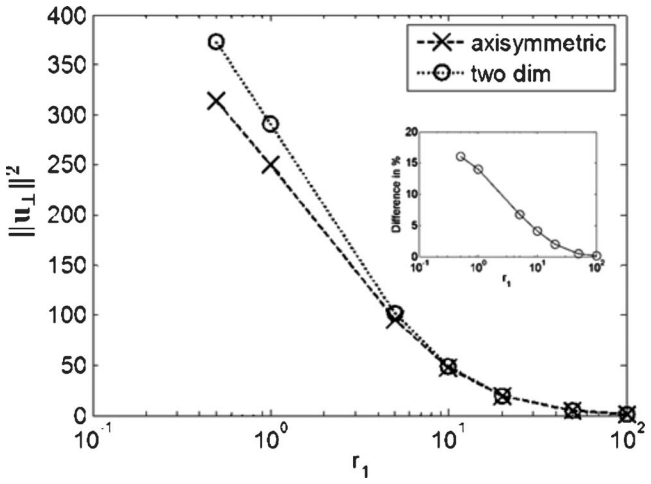

FIG. 12. The kinetic energy of the secondary flow $\|\mathbf{u}_\perp\|^2$ as a function of r_1. $D_1 = D_2 = 1$. $j^* = 0.15$. $l = 2$. The dotted line with circles corresponds to results of the simplified, two-dimensional model. The dashed line with crosses shows results of the axisymmetric model. The inset depicts the relative difference between the approximate model and exact model predictions as a function of r_1.

The continuity equation is

$$\frac{\partial u}{\partial r} + \frac{\partial w}{\partial z} = 0. \tag{60}$$

Additionally, one needs to solve the Nernst-Planck equations (14) and (15) for the concentration field.

We characterize the intensity of the secondary flow in the $r - z$ plane with its kinetic energy

$$\|\mathbf{u}_\perp\|^2 = \iint \left(u^2 + w^2\right) dx dz. \tag{61}$$

Figure 12 depicts $\|\mathbf{u}_\perp\|^2$ as a function of the curvature r_1 when $l = 2$. Non-slip boundary conditions are imposed at $z = 0$ and $z = l$. The crosses and circles correspond, respectively, to axisymmetric and two-dimensional predictions. The inset depicts the relative difference (%) between the axisymmetric and two-dimensional simulations as a function of r_1. When $r_1 > 40$ (curvature of 0.025), the difference between the two models' predictions is smaller than 1%. The two-dimensional model overestimates the kinetic energy of the secondary flow. This is consistent with results previously obtained for pressure-driven Dean flow. Finlay and Nandakumar[43] and Yanase *et al.*[44] argued, respectively, that the Dean approximation is applicable when the curvature is smaller than 0.1 and 0.01.

B. The effect of current direction on secondary convection

A somewhat unexpected result of our linear stability analysis is the strong dependence of the stability characteristics on the direction of the current flow. Outwardly directed current destabilizes the azimuthal flow and leads to early evolution of secondary flows, while inwardly directed current suppresses secondary convection. While in the infinitely long annulus secondary flows evolve only when the current is directed outwardly, the situation is quite different in the case of the finite-height annulus. As we have noted earlier, when the annulus is of finite height, secondary flows will always be present, regardless of the current's direction. These secondary flows are due to pressure gradients caused by the non-slip floor and ceiling.

Figure 13 depicts the flow patterns and the concentration distributions (a and b) and the current flux intensities (c and d) when the current is controlled and directed inwardly (a and c) and when the current is directed outwardly (b and d). The streamlines are shown with solid lines and the

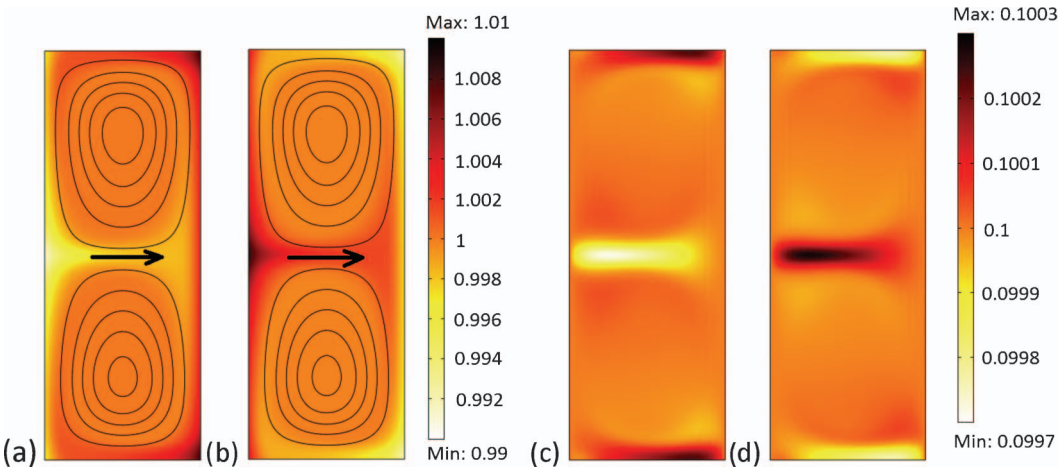

FIG. 13. (Color online) MHD flow in an annulus of height $l = 2\pi/2.39$. (a) Concentration distribution c_1 and the (u, w) streamlines (solid lines) when $j^* = -0.1$. (b) Concentration distribution c_1 and the (u, w) streamlines (solid lines) when $j^* = 0.1$. (c) Intensity of electric current flux distribution in case (a). (d) Intensity of electric current flux distribution in case (b). All the other parameters are the same as used in Figure 7.

concentration and current flux intensities are color coded with light color and dark color indicating, respectively, low and high magnitudes. See keys to the right of the figures. The annulus height $l = 2\pi/2.39$. No-slip conditions are specified at $z = 0$ and $z = l$. All other conditions are the same as in Figure 7. In both cases, the secondary flow is such that the velocity at the mid-height plane is directed towards the outer cylinder. The fluid returns towards the inner cylinder next to the top and bottom boundaries. When the current is directed outwardly, the ion concentrations are higher close to the inner cylinder's surface. These ions are advected outwardly, forming a higher concentration/higher electric conductivity "plume" at the annulus' mid-height plane, which results in a higher current density, a larger Lorentz force, and enhanced azimuthal velocity (Figure 13(a)). In contrast, when the current is directed inwardly, the mid-height plane contains fewer ions than in the absence of secondary flows (Figure 13(b)) and the driving force is slightly reduced. As a result, the azimuthal velocity in the case of the outwardly directed current is slightly larger than in the case of the inwardly directed current.

Similar behavior is observed when the electrodes' potential difference is controlled. To characterize the intensity of the secondary flow, we use the two-dimensional kinetic energy $\|\mathbf{u}_\perp\|^2$ (Eq. (61)). Figure 14 depicts $\|\mathbf{u}_\perp\|^2$ as a function of the applied external potential difference ΔV_{ext} when the electrodes' potential difference is controlled. The solid line with crosses denotes an infinite annulus with $k = 4$. The dashed lines with squares, circles, and triangles correspond to finite annuli with $l = \pi$, $\pi/2$, and $\pi/4$. For conditions similar to the ones specified in Figure 10, $\Delta V_{ext} = 11.32$, and the resulting average current flux $|j^*| = 0.1$. When the current is positive (negative), the intensity of the secondary flows $\|\mathbf{u}_\perp\|^2 = 0.2850$ (0.2832). In the equivalent pressure-driven flow (with the same average azimuthal velocity), $\|\mathbf{u}_\perp\|^2 = 0.2843$. Witness that $\|\mathbf{u}_\perp\|^2_{positive\ \Delta V_{ext}} > \|\mathbf{u}_\perp\|^2_{pressure\ driven} > \|\mathbf{u}_\perp\|^2_{negative\ \Delta V_{ext}}$ and $\|\mathbf{u}_\perp\|^2_{Finite\ Annulus} > \|\mathbf{u}_\perp\|^2_{Infinite\ Annulus}$.

Figures 15(a)–15(c) depict, respectively, the secondary flow's intensity $\|\mathbf{u}_\perp\|^2$, the average azimuthal velocity $\bar{v}$, and the average current density $\bar{j}$ as functions of the aspect ratio l ($0.63 < l < 3.14$). The dashed lines and the hollow circles correspond, respectively, to the case of $\Delta V_{ext} = 15$ and the case of $\Delta V_{ext} = -15$. Figure 15(d) depicts the relative differences (%) between secondary flow intensity (dashed line), average azimuthal velocity (solid line), and average current flux (dashed line) when the current is positive and when the current is negative as functions of the annulus aspect ratio l.

In contrast to the case of the infinitely tall annulus, when the annulus' height is finite, the differences between the outwardly and inwardly directed currents are relatively small. This is

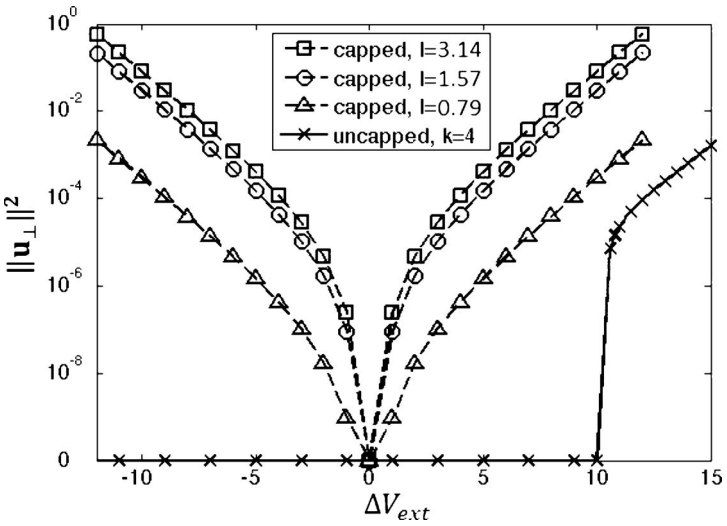

FIG. 14. The intensity of the secondary flow $\|\mathbf{u}_\perp\|^2$ (Eq. (61)) as a function of the potential difference between the electrodes (ΔV_{ext}). The dashed line with squares, the dashed line with circles, and the dashed line with triangles correspond, respectively, to capped conduits with heights π, $\pi/2$, and $\pi/4$. The solid line with crosses corresponds to an infinitely long, annular conduit with periodic boundary conditions in the axial (z) direction and wave number $k = 4$. All the other parameters are the same as in Figure 10.

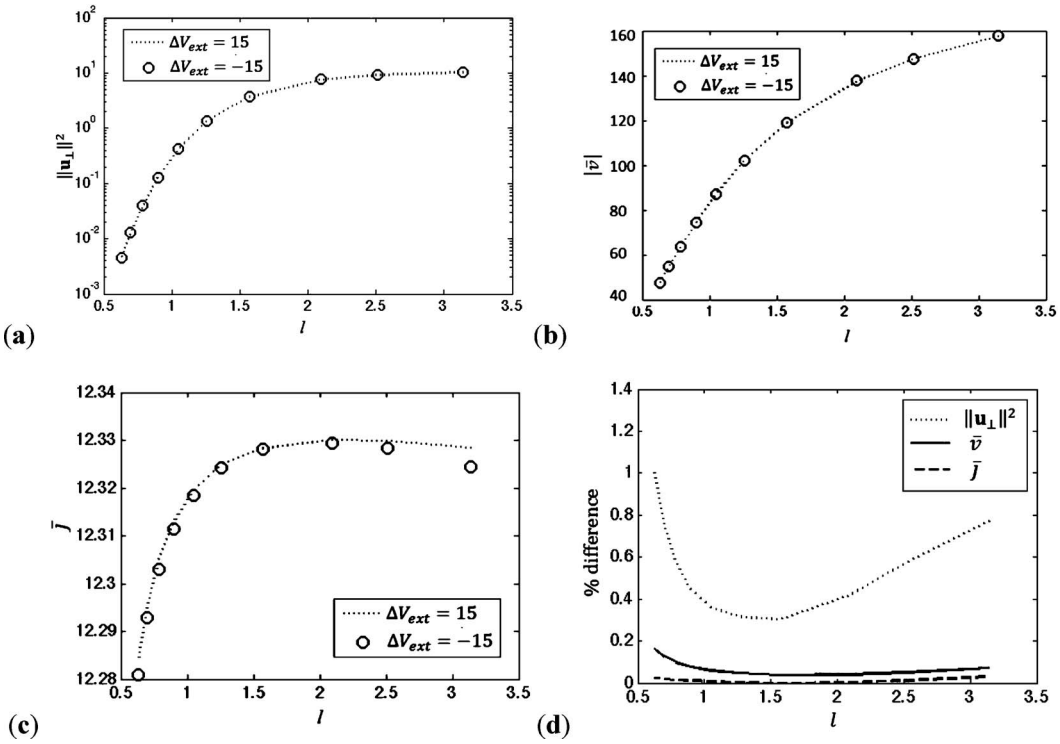

FIG. 15. The intensity of the secondary flow $\|\mathbf{u}_\perp\|^2$ (a), the average azimuthal velocity $|\bar{v}|$ (b), and the average current flux (c) as functions of the aspect ratio l when the potential is controlled. The dashed line and the hollow circles correspond, respectively, to positive ($\Delta V_{ext} = 15$) and negative ($\Delta V_{ext} = -15$) currents. (d) The relative difference between the intensity of the secondary flow $\|\mathbf{u}_\perp\|^2$ (dashed line), average azimuthal velocity (solid line), and average current flux as functions of the aspect ratio l.

because the secondary flow is primarily driven by the pressure gradients induced by the floor and ceiling and only weakly modified by the Dean instability.

VI. CONCLUSIONS

In this study, we provided base solutions of concentration distributions, velocity profiles, and current flux fields of MHD flow in an annular conduit when the cylinders are infinitely long. The azimuthal flow is similar to the celebrated Dean flow. In contrast to the Dean flow, the MHD flow described here can actually be attained in practice.

We examined, for the first time, the linear stability of the azimuthal flow in the infinitely long annulus. The disturbance growth rate at loss of stability was always real and the principle of exchange of stability holds. We delineated the effect of electrochemistry on the Dean instability. When the current flow was directed outwardly (positive), electrochemical effects destabilized the azimuthal flow. The bifurcation into secondary, cellular convection (in the radial plane) occurred at a much smaller Dean number than in the pressure-driven case. When the current was directed inwardly (negative), the azimuthal flow was linearly stable for *all* Dean numbers. In other words, when the current was directed inwardly, electrochemical effects stabilized the flow.

The predictions of the linear stability analysis were compared and favorably agreed with finite element solutions of the nonlinear problem. Consistent with linear stability theory, the nonlinear simulations indicate that the disturbances grow/decay monotonically and that the bifurcation in the case of outwardly directed current is supercritical.

Finite element analysis was also carried out to study the magnetohydrodyamic flow in the capped (finite length) annulus. When the annulus is of finite height, pure azimuthal flows are inadmissible and the flow is always three-dimensional, regardless of the direction of the current. The secondary flow is primarily caused by pressure gradients induced by the presence of the floor and ceiling (due to the non-slip boundary condition at these boundaries) and the Dean instability plays a relatively minor role in modifying the flow field. As a result, the differences in the intensity of the secondary convection between the outwardly directed current and inwardly directed current are relatively small, albeit the intensity of the secondary convection is always greater in the case of the outwardly directed current.

ACKNOWLEDGMENTS

The work was supported, in part, by NSF STTR Grant No. 0822723 to SFC Fluidics.

[1] S. Qian and H. H. Bau, "Magneto-hydrodynamics based microfluidics," Mech. Res. Commun. **36**, 10 (2009).
[2] W. R. Dean, "Fluid motion in a curved channel," Proc. R. Soc. London, Ser. A **121**, 402 (1928).
[3] H. Ito, "Theory on laminar flow through curved pipes of elliptic and rectangular cross-section," Rep. Inst. High Speed Mech., Tohoku Univ. **1**, 1 (1951).
[4] S. Chandrasekhar, *Hydrodynamic and Hydromagnetic Stability* (Clarendon, Oxford, London, 1961), pp. 343–379.
[5] P. G. Drazin and W. H. Reid, *Hydrodynamic Stability* (Cambridge University Press, London, 2010), pp. 108–112.
[6] K. H. Winters, "A bifurcation study of laminar flow in a curved tube of rectangular cross-section," J. Fluid Mech. **180**, 343 (1987).
[7] B. Bara, K. Nandakumar, and J. H. Masliyah, "An experimental and numerical study of the Dean problem: flow development towards two-dimensional multiple solutions," J. Fluid Mech. **244**, 339 (1992).
[8] S. A. Berger and L. Talbot, "Flow in curved pipes," Annu. Rev. Fluid Mech. **15**, 461 (1983).
[9] W. Y. Soh, "Developing fluid flow in a curved duct of square cross-section and its fully developed dual solutions," J. Fluid Mech. **188**, 337 (1988).
[10] P. H. M. Bovendeerd, A. A. Van Steenhoven, F. N. Van de Vosse, and G. Vossers, "Steady entry flow in a curved pipe," J. Fluid Mech. **177**, 233 (1987).
[11] M. Boutabaa, L. Helin, G. Mompean, and L. Thais, "Numerical study of Dean vortices in developing Newtonian and viscoelestic flows through a curved duct of square cross-section," C. R. Mec. **337**, 40 (2009).
[12] K. C. Cheng, R. C. Lin, and J. W. Ou, "Fully developed laminar flow in curved rectangular channels," J. Fluid Eng. **98**, 41 (1976).
[13] A. C. Verkaik, B. W. A. M. M. Beulen, A. C. B. Bogaerds, M. C. M. Rutten, and F. N. van de Vosse, "Estimation of volume flow in curved tubes based on analytical and computational analysis of axial velocity profiles," Phys. Fluid **21**, 023602 (2009).
[14] H. G. Cuming, "The secondary flow in curved pipes," Aeronautical Research Council Reports Memoranda No. 2880, 1995.

[15] R. J. Silva, R. M. Valle, and M. Ziviani, "Numerical hydrodynamic and thermal ananlysis of laminar flow in curved elliptic and rectangular ducts," Int. J. Therm. Sci. **38**, 585 (1999).
[16] J. A. C. Humphrey, A. M. K. Taylor, and J. H. Whitelaw, "Laminar flow in a square duct of strong curvature," J. Fluid Mech. **83**, 509 (1977).
[17] M. J. Targett, W. B. Retallick, and S. W. Churchill, "Flow through curved rectangular channels of large aspect ratio," AIChE J. **41**, 1061 (1995).
[18] H. J. De Vriend, "Velocity redistribution in curved rectangular channels," J. Fluid Mech. **107**, 423 (1931).
[19] S. Yanase, Y. Kaga, and R. Daikai, "Laminar flows through a curved rectangular duct over a wide range of the aspect ratio," Fluid Dyn. Res. **31**, 151 (2002).
[20] A. A. Avramenko, S. G. Kobzar, I. V. Shevchuk, A. V. Kuznetsov, and B. I. Basok, "Laminar forced convection in curved channel with vortex structures," J. Therm. Sci. **13**, 143 (2003).
[21] K. C. Cheng and M. Akiyama, "Laminar forced convection heat transfer in curved rectangular channels," Int. J. Heat Mass Transfer. **13**, 471 (1970).
[22] T. W. Gyves and T. F. Irvine, Jr., "Laminar conjugated forced convection heat transfer in curved rectangular channels," Int. J. Heat Mass Transfer. **43**, 3953 (2000).
[23] R. N. Mondal, M. S. Uddin, and A. Islam, "Non-isothermal flow through a curved rectangular duct for large Grashof number", J. Phys. Sci. **12**, 109 (2008).
[24] J. Zhong, M. Yi and H. H. Bau, "A magneto-hydrodynamics (MHD) pump fabricated with ceramic tapes," Sen. Actuators, A **96**(1), 59 (2002).
[25] J. C. T. Eijkel, C. Dalton, C. J. Hayden, J. P. H. Burt, and A. Manz, "A circular ac magnetohydrodynamic micropump for chromatographic applications," Sen. Actuators, B **92**, 215 (2003).
[26] E. P. Velikhov, "Stability of an ideally conducting liquid flowing between cylinders rotating in a magnetic field," Sov. Phys. J. Exp. Theor. Phys. **36**, 995 (1959).
[27] I. V. Khalzov, V. I. Ilgisonis, A. I. Smolyakov, and E. P. Velikhov, "Magnetorotational instability in electrically driven flow of liquid metal: Spectral analysis of global modes," Phys. Fluid **18**, 124107 (2006).
[28] J. C. R. Hunt and W. E. Williams, "Some electrically driven flows in magneto-hydrodynamics. Part I. Theory", J. Fluid Mech. **31**, 705 (1968).
[29] J. C. R. Hunt and D. G. Malcolm, "Some electrically driven flows in magnetohydrodynamics. Part II. Theory and Experiment," J. Fluid Mech. **33**, 775 (1968).
[30] J. C. R. Hunt and K. Stewartson, "Some electrically driven flows in magneto–hydrodynamics. Part III. The asymptotic theory for flow between circular electrodes," J. Fluid Mech. **38**, 225 (1969).
[31] J. A. Baylis, "Detection of the onset of Instability in a cylindrical magnetohydrodynamic flow," Nature (London) **204**, 563 (1964).
[32] J. A. Baylis, "Experiments on laminar flow in curved channels of square section," J. Fluid Mech. **48**, 417 (1971).
[33] R. Kobayashi, "Stability of MHD viscous flow in a curved channel," Bull. JSME **20**, 983 (1977).
[34] M. Qin and H. H. Bau, "When MHD-based microfluidics is equivalent to pressure-driven flow," Microfluid. Nanofluid. **10**(2), 287 (2011).
[35] G. Marshall and P. Mocskos, "Growth model for ramified electrochemical deposition in the presence of diffusion, migration, and electroconvection," Phys. Rev. E **55**, 549 (1997).
[36] D. R. Laughlin, "Magnetohydrodynamic (MHD) actuator sensor," U.S. patent 7,171,853 (2007).
[37] V. M. Volgin and A. D. Davydov, "Natural-convective instability of electrochemical systems: A Review," Russ. J. Electrochem. **42** 567 (2006).
[38] J. Newman and K. E. Thomas-Alyea, *Electrochemical Systems* (Wiley, Englewood Cliffs, NJ, 2004), pp. 186–208.
[39] A. J. Bard and L. R. Faulkner, *Electrochemical Methods, Fundamentals and Applications* (Wiley, Hoboken, NJ, 2001), pp. 87–107.
[40] S. Qian, Z. Chen, J. Wang, and H. H. Bau, "Electrochemical reaction with RedOx electrolyte in toroidal conduits in the presence of natural convection," Intl. J. Heat Mass Transfer. **49**, 21 (2006).
[41] S. Goldstein, *Modern Developments in Fluid Dynamics* (Clarendon, Oxford, London, 1938), pp. 312–315.
[42] R. M. Digilov, "Making a fluid rotate: Circular flow of a weakly conducting fluid induced by a Lorentz body force," Am. J. Phys. **75**, 361 (2007).
[43] W. H. Finlay and K. Nandakumar, "Onset of two-dimensional cellular flow in finite curved channels of large aspect ratio," Phys. Fluid A **2**, 1163 (1990).
[44] S. Yanase, K. Yamamoto, and T. Yoshida, "Effect of curvature on dual solutions of flow through a curved circular tube," Fluid Dyn. Res. **13**, 217 (1994).